Generation of γ-Alumina Digital Twins using a Nitrogen Porosimetry Simulation

Gabriel Alejandro Ledezma Lopez, Jan J. Verstraete, Loïc Sorbier, Aleksandra Glowska, Damien Leinekugel-Le-Cocq, Elsa Jolimaitre, Christian Jallut

Generation of γ-alumina digital twins using a nitrogen porosimetry simulation

*G. Ledezma[ab], J.J. Verstraete[a], L. Sorbier[a], A. Glowska[ac], D. Leinekugel-Le Cocq[a], E. Jolimaitre[a], C.Jallut[b]

a IFP Energies nouvelles, Rond-point de l'échangeur de Solaize, BP 3, 69360 Solaize, France

b Univ Lyon, Université Claude Bernard Lyon 1, CNRS, LAGEPP UMR 5007 43 boulevard du 11 novembre 1918, Villeurbanne, F-69100, France.

c Centre for Nature Inspired Engineering (CNIE), University College of London, Gower Street, London, WC1E6BT.

*Corresponding author E-Mail: gabriel-alejandro.ledezma-lopez@ifpen.fr

Abstract

A γ-alumina digital twin is created by means of a hierarchical pore network model. For this digital twin, nitrogen porosimetry is simulated, and the parameters of the pore network model are modified by means of a particle swarm optimization (PSO) algorithm until both branches of the digital isotherm match those of the experimental isotherm. After parameter identification, the resulting pore network model provides a digital isotherm that is in good agreement with the experimental results. The same set of parameters also allows to predict the experimental nitrogen scanning curves. The BJH pore size distribution obtained from the digital isotherm corresponds well to the experimental one. Therefore, the generated digital twin can statistically represent the topology of the industrial alumina sample. Diffusion simulations on the final structure allowed to estimate the tortuosity factor of the structure. The predicted value differs by less than 20% from the tortuosity factor measured by PFG-NMR.

Keywords

Nitrogen Adsorption; Pore Network Models, Computational Characterization; Gamma Alumina Supports, Digital Twin.

1. Introduction

Porous materials are widely used in chemical engineering. On the mesoporous scale, the confinement effects influence the thermodynamics and transport conditions. Indeed, the architecture of the porous material can enhance mass transfer limitations inside of the catalyst (*39*). Therefore, understanding not just the textural properties but also the topology of the solid is important to improve the catalyst performance and the accuracy of different models. This makes it possible to design and evaluate heterogeneous reactor performances (*40–42*).

Modeling the phenomena that occur in the interior of the pore network can improve the assessment of critical descriptors that are valuable for the synthesis of industrial catalysts, supports, and adsorbents. When applied to chemical reactors or adsorbers, it would then be possible to (i) estimate the tortuosity of a catalyst sample through computer simulations starting from inexpensive and common characterization techniques, and (ii) optimize the structural parameters of the γ-alumina to maximize activity, selectivity and/or stability of the catalyst.

In order assess the phenomena that occur in the interior of the porous structure, it is possible to use either mimetic methods or reconstruction methods (*1*). Mimetic methods try to create the final material by simulating its synthesis, starting from the genesis all the way to the final structure of the solid. On the other hand, reconstruction methods directly model the material in its final state. Among the reconstruction methods, pore network models are common representations. They are widely used because of their ease of construction, flexibility, and reasonable computer processing unit (CPU) intensity. Such structures represent a useful solution for adsorption, dissolution and precipitation (*2*), biomass growth (*3*), permeability (*4*), carbon capture (*5*), fuel cells (*6*), adsorbers (*7*), and chemical reactors (*8, 9*). Pore network models were mentioned for the first time by Fatt in 1956 (*10*). At that

time, the novelty resided in the consideration of the pore network connectivity that was lacking in the classic “bundle of tubes” model (*11*). Since then, multiple variants have been proposed to understand the role of the different characteristics of the network architecture on thermodynamics and transfer phenomena. Proposed modifications consider different textural and topological characteristics that can be relevant to describe the material. Amongst the more relevant improvements are the dual site bond model (DSBM), proposed by Cruz in 1989 (*12*–*14*) and later modified by Riccardo, to create energetically consistent structures (*15*). The corrugated pore structure model (CPSM), first proposed by Mann and Andropoutsopoulus in 1981 (*16*–*18*), accounts for the rugosity on the pore walls. Hierarchical pore network models were described in the works from Spearing and Matthews, Rieckmann, Gladden, Sharrat and Hollewand, and Sadeghi (*19*–*24*). These works studied the link between hierarchical structure, the tortuosity factor, and the effectiveness factor.

To correctly model the heterogeneity of the solid, the needed experimental data can come from Small Angle X-ray Scattering (SAXS), X-ray computed microtomography (micro-CT), Focused Ion Beam (FIB) coupled with Scanning Electron Microscopy (SEM), Nuclear Magnetic Resonance (NMR)-Relaxometry, Nuclear Magnetic Resonance-Cryoporometry, mercury porosimetry, and nitrogen porosimetry.

In many cases, only nitrogen and mercury porosimetry are available because these techniques are the fastest, least expensive, and most common techniques that provide qualitative information on the topology and the architecture of the network. Hence, many studies have been conducted on the different scales to improve the understanding and quality of the models used for the interpretation of the experimental data from nitrogen porosimetry. Molecular simulations in a single pore helps to understand the effect of the confinement on the gas adsorption/condensation and evaporation/desorption (*25*–*29*). Other studies try to explain the effect of the connectivity and the architecture (*30*–*38*) on reaction and transport properties at the mesoscopic scale. There are also studies at the mesoscopic-macroscopic scales that try to explain the shape of the catalyst pellet.

γ-alumina is a disordered porous material with an elevated tortuosity very often used in oil refining and petrochemistry, whose topology is not yet fully understood (*1, 43, 44*). Recent research articles propose that this material has different pore domains, each one characterized by its own pore size distribution and void fraction (*45*). The interplay among these different levels clearly plays a role in effective diffusion. By creating digital twins of real γ-alumina samples, it is possible to better understand how the textural properties and the topology of the network influence diffusion through the network at a fundamental level. At the same time, in applied research and development, this allows one to create more accurate and flexible models that better represent the reactor performance. In this paper, a methodology to create a γ-alumina digital twin able to reproduce experimental nitrogen isotherms and the scanning curves associated to the same sample is proposed and tested. A semi-infinite cube simulation is performed on the final structure to calculate the tortuosity factor associated with it.

2. Alumina synthesis and characterization

Nitrogen adsorption-desorption isotherms of various γ-aluminas were measured on the 3Flex instrument (Micromeritics). Prior to analysis, the samples were subjected to a pretreatment at 350°C during 3 hours under secondary vacuum (10^{-5} mbar). Structural properties, such as porous volume and specific surface area, were evaluated from the nitrogen adsorption isotherm with an expected uncertainty of 3% and 5%, respectively. For evaluation of pores size distribution, the BJH model was used. The analysis was repeated several times on each alumina sample for measurement of desorption scanning isotherms. Each scanning curve was measured by allowing adsorption up until a fixed value of relative pressure below 1, followed by complete desorption induced through gradual decrease of pressure.

Helium pycnometry was performed on the AccuPyc 1340 apparatus (Micromeritics) to evaluate the structural density of each alumina (ρ_s), which was further used to calculate the total porosity (ε_{N2}) from the porous volume provided by nitrogen adsorption according to the following expression:

$$\varepsilon_{N_2} = \frac{V_{pore}}{V_{pore} + \frac{1}{\rho_s}}$$

(1)

Diffusion measurements were performed by ^{1}H Pulsed-Field Gradient (PFG)-NMR at 305 K on an Avance 600 MHz spectrometer (Bruker) equipped with a BBI (Double Resonance Broadband Probe) scattering probe of 5 mm and a field gradient amplifier capable of producing field gradient pulses up to 50 G/cm. A range of organic liquids of varying size and polarity were used for experiments (Table 1), and, for each molecule, the unrestricted molecular and effective self-diffusivity in the support was measured.

Table 1. Molecular size and dipole moment of organic liquids used for diffusion measurements

Organic liquid	Formula	Molecular radius (Å)	Dipole moment (D)
Acetonitrile	C_2H_3N	2.76	3.30
Toluene	C_7H_8	3.49	0.36
n-Heptane	C_7H_{16}	3.89	0
Squalane	$C_{30}H_{62}$	5.94	0
Perfluorooctane	C_8F_{18}	4.63	0

For molecular and effective self-diffusion measurements, a 13-interval stimulated echo-pulsed bipolar sequence (PGSTEBP, Bruker) was applied with the acquisition parameters mentioned in Table 2.

Table 2. Acquisition parameters for PFG-NMR experiments

PFG-NMR parameter	Unrestricted molecular diffusion	Effective diffusion in support
Diffusion time Δ (s)	0.140	
Gradient pulse duration δ (s)	$6 \cdot 10^{-4}$	
Gyromagnetic ratio of ^{1}H, γ_g (rad·s^{-1}·G^{-1})	$2.67 \cdot 10^{4}$	
Time between two radio-frequency pulses τ_e (s)	$2.61 \cdot 10^{-3}$	
Maximum gradient intensity *G* (G/cm)	26	46
Number of gradient steps (-)	10	20

In both cases, measurements were conducted through linear variation of the gradient intensity *G* at a constant gradient pulse duration δ. For the PGSTEBP sequence, the relation between signal intensity and the self-diffusion coefficient for a molecule *i* (D_i) is expressed as:

$$I = exp\left[-\left(\gamma_g \delta G\right)^2 D_i \left(4\Delta + 6\tau_e - \frac{2\delta}{3}\right)\right] \quad (2)$$

where D_i represents either the molecular D_m or effective diffusivity D_{eff}, depending if diffusion is measured for unconfined molecules in the bulk or within the porous solid, respectively.

Prior to PFG-NMR experiments on the studied alumina, support extrudates were dried at 120°C for 24 h in order to remove physisorbed water. Directly after pretreatment, the extrudates were soaked in each organic liquid for 10 minutes to ensure full saturation. Before analysis, extrudates were taken out from the liquids and gently rolled over blotting paper to remove excess liquid from the external extrudate surface. All measurements were performed in 5 mm NMR tubes on a single extrudate placed in a 2.5 mm capillary and the analysis was repeated on three extrudates for each studied liquid to verify the repeatability of effective diffusivity measurement.

Based on these measurements, the tortuosity factor (τ) was calculated for each liquid as the ratio of the unrestricted molecular diffusivity to the effective diffusivity in alumina:

$$\tau = \frac{D_m}{D_{eff}} \tag{3}$$

3. Simulation

The objective of this work is to generate a pore network model that recreates the topology of the real industrial alumina sample. To do this, the simulations are decomposed into two main blocks: pore network generation and nitrogen sorption simulation. If the obtained digital isotherm does not fit the experimental curve, then the input parameters used for the generation of the pore network model are changed (Figure 1).

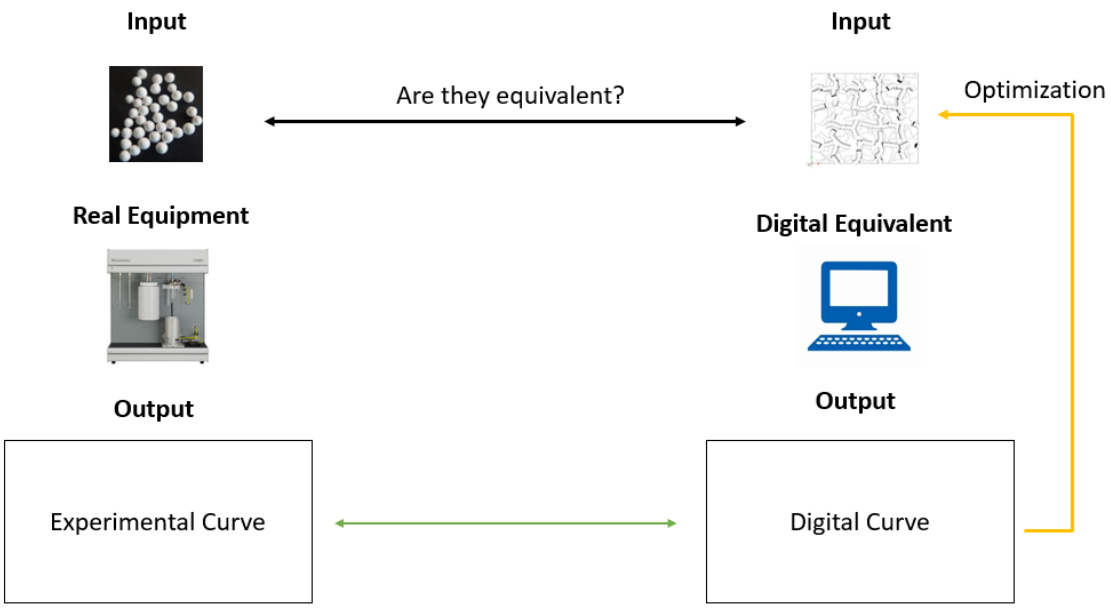

Figure 1. Comparison of the common experimental and digital steps for nitrogen characterization.

3.1 Pore Network Model

The pore network model is created through a discrete reconstruction method based on a stochastic algorithm. In this model, the pores are represented by hollow cylinders that connect two nodes. The

nodes can be set to have zero volume (the nodes do not play any physical role) or can be modeled as hollow spheres that have physical influence in the model (Figure 2).

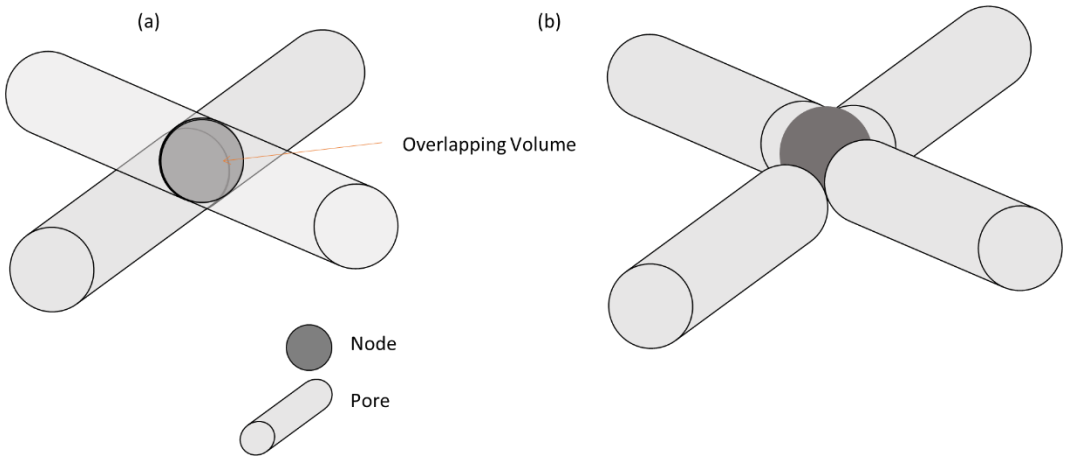

Figure 2. Schematic representation of an elementary node-pore system for a square lattice with Pore Existence Probability (PEP) equal to 1. (a) The porous space is represented by the cylinders. (b) The porous space is represented by the cylinders and the nodes (*46*).

For the stochastic construction of the network, the pores are distributed in a lattice. The characteristics of this lattice will set the maximum connectivity of the network. Different features provide heterogeneity to the digital structures in order to get not only a good representation of the textural properties but also a good representation of the topology of the network. With the developed simulation tool, it is possible to use several pore size distributions in the same network, which allows the construction of hierarchical structures, i.e. networks with different porosity levels. The porosity of each porosity level of the network is regulated through a threshold value defined as pore existence probability (PEP). Each porosity level can have its own PEP. Also, the length of the pores can either be constant in regular lattices, or variable by creating random distortions in the lattice. The grid spacing between the different pore levels can also be modified, defining their intertwining and adding complexity to the final network. It is possible to create a pore network in 1D, 2D or 3D. In Figure 3, different transversal sections of different pore networks are illustrated. Figure 3a and Figure 3b were created using a regular lattice with two porosity levels with different pore size distributions and a grid spacing of 6 between them. In Figure 3b a distorted lattice has been used. Figure 3c, Figure 3d, Figure 3e, and Figure 3f were created using five different pores size distributions and a complex grid spacing

combination between them. Figure 3b, Figure 3d, Figure 3f are distorted, contrary to their counterparts Figure 3a, Figure 3c, and Figure 3e.

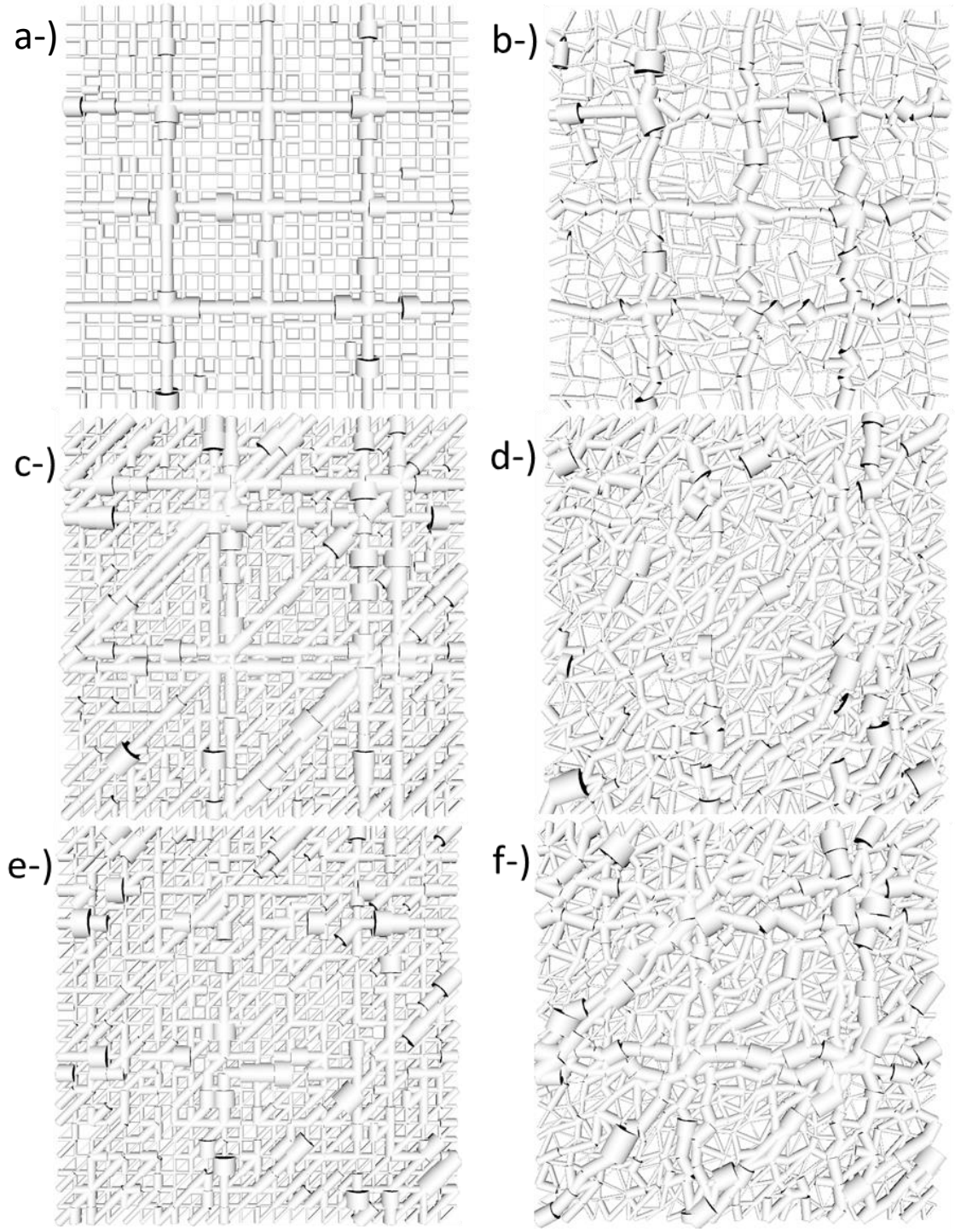

Figure 3. Transversal section of 6 different pore network: a-) Pore network created with 2 different pore size distributions, a space grid equal to 6 for the second population, and PEP 1. b-) Distorted pore network created with 2 different pore size distributions, a space grid equal to 6 for the second population, and PEP 1. c-) Pore network created with 5 different pore size distributions and PEP 1 for all the populations. d-) Distorted Pore network created with 5 different pore size distributions and PEP 1 for all the populations. e-) Pore network created with 5 different pore size distributions and PEP 0.5 for the population of pores with higher diameter. f-) Distorted pore network created with 5 different pore size distributions and PEP 0.5 for the population of pores with higher diameter.

3.2 Nitrogen Sorption

Nitrogen sorption is a classical characterization technique that is used to obtain information about the textural properties of porous solids. The methodology used for the nitrogen porosimetry simulation was already described in one of our previous publications (*46*). However, it will be briefly summarized here. There are two main stages to model, the adsorption stage and the desorption stage. There is a fundamental difference that arises between the two stages. During adsorption, the phase change pressure is not dependent on the position of the pore in the pore network. Hence, the description of the thermodynamic phenomenon in each pore is simply governed by its actual pore diameter. However, during the desorption stage, the phase change pressure is dependent on the position of the pore in the pore network. In a cylindric pore, the equilibrium pressure depends upon the diameter of the pore. During desorption, a gas-liquid interphase is necessary to allow for the evaporation of the nitrogen inside of the pore once the equilibrium pressure is reached. However, if a pore is surrounded at both ends with smaller pores that are still full of liquid nitrogen, because of their lower desorption pressure, then the nitrogen contained inside of this central pore will be blocked until the lower desorption pressure of the smaller neighboring pores is reached. This phenomenon is usually called pore blocking and must be included in the model for the desorption stage, in addition to the thermodynamic phenomena of the system.

To model nitrogen porosimetry, the following assumptions made are (*46*):

- The pores are rigid.
- All pores are open at both ends.
- The adsorption mechanism starts with the adsorption of the nitrogen on the walls followed by sudden condensation.
- The phase change pressure is governed by capillary forces and the blocking pore phenomena.
- The meniscus shape is cylindrical both for adsorption and desorption.

- The condensed nitrogen must be in contact with the vapor phase for evaporation to occur.
- The pore-blocking phenomenon is only dependent on the topology of the system.
- The pore size distribution is within the mesopore range.
- The system is in equilibrium.
- No cooperative effects other than contact with vapor phase are considered.

3.2.1 Thermodynamic model

The Kelvin equation (4) represents the thermodynamics of the vapor-liquid equilibrium in a confined medium. It relates the pore size to the pressure at which phase change occurs at constant temperature. In equation 4, σ_{lg} represents the liquid-gas surface tension, $r_1(t)$ and $r_2(t)$ represent the meniscus curvature radius, V_{lm} is the liquid molar volume, and P is the equilibrium pressure. In the literature, the shape of the menisci has been proposed to be cylindrical during the adsorption process (5) and hemispherical during the desorption process ((6), although this also depends on whether the pore is open at both ends or not (*26, 47, 25, 48*). In the results presented in this paper, the menisci are always considered to be cylindrical. Thus, the hysteresis loop is purely caused by the pore blocking effect.

While the Kelvin equation models the core condensation, the Harkins-Jura statistical thickness equation (7) is used to model the thickness of the adsorbed nitrogen layer on the pore walls prior to the core condensation (or after the core vaporization).

$$\frac{P}{Po} = \exp\left(\frac{-\sigma_{lg} * V_{lm}}{RT} * \left(\frac{1}{r_1(t)} + \frac{1}{r_2(t)}\right)\right)$$

(4)

$$\frac{P}{Po} = \exp\left(\frac{-\sigma_{lg} * V_{lm}}{RT} * \left(\frac{1}{r_{\mathrm{eq}}(t)}\right)\right)$$

(5)

$$\frac{P}{Po} = \exp\left(\frac{-\sigma_{lg} * V_{lm}}{RT} * \left(\frac{2}{r_{\mathrm{eq}}(t)}\right)\right)$$

(6)

$$t = \frac{13.99}{0.034 - log_{10}\left(\frac{P}{P^0}\right)}^{\frac{1}{2}}$$

(7)

3.2.2 Pore Blocking Phenomena

Because of pore blocking phenomena, desorption does not always happen at the pressure that corresponds to the diameter of the pore, but it can occur at pressures that correspond to a lower diameter. As explained above, this is the case if a pore is surrounded at both ends with smaller pores. Since these neighboring pores can in turn be blocked by even smaller pores, pore blocking will propagate throughout the entire pore network model. An algorithm was developed (*46*) to determine the pressure at which a cylindrical pore will empty through the pore network, and this information is stored as an equivalent desorption diameter, called “desorption triggering diameter”. This desorption triggering diameter is the diameter that corresponds to the desorption equilibrium pressure at which a given pore will empty, according to its position inside the network.

3.2.3 Isotherm generation

For the generation of the adsorption branch of the isotherm, the volume adsorbed/condensed at each pressure step for each pore must be quantified. If the diameter of the pore (D_p) is higher than the equilibrium diameter (D_{eq_n}-2t) for a given relative pressure, then the adsorbed nitrogen volume in a pore at the current pressure will be equal to:

$$V_{cum(@p_i)} = \pi * l * \left(D_p - t\right) * t$$

(8)

However, if ($D_p < D_{eq\_n}$-2t), it is considered that core volume has already condensed and the volume of liquid in the pore is simply equal to:

$$V_{cum(@p_i)} = \frac{\pi}{4} * l * D_p^2$$

(9)

The desorption branch is simulated using again the equation *(5)*, but this time, it is necessary to consider the pore blocking phenomena. Then, to know whether equation *(9)* or equation (*8)*

should be used, the procedure is the same as for adsorption but the desorption triggering diameter (D_T) is used instead of the actual diameter (D_p) in the comparison against the equilibrium diameter (D_{eq_n}-2t) for each given pressure step. The algorithm tree is shown in Figure 4.

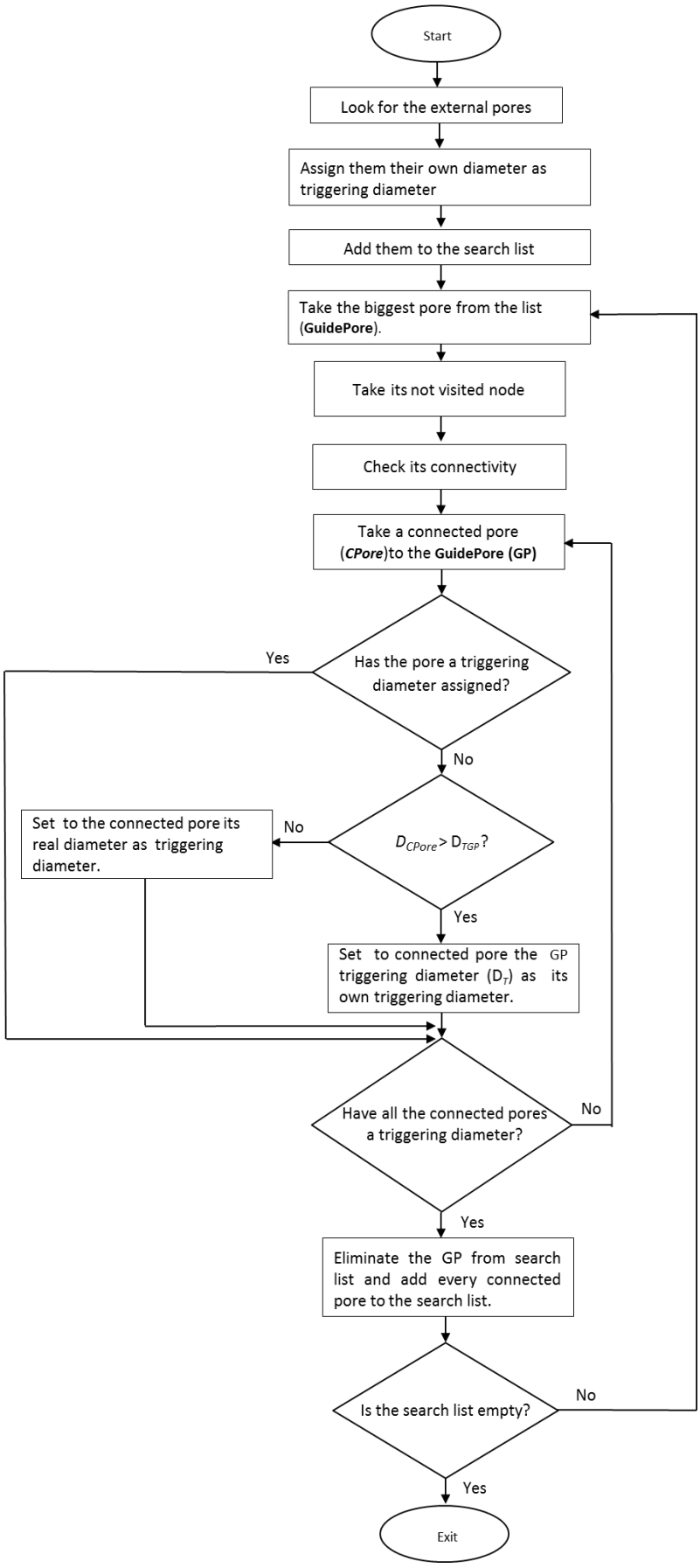

Figure 4. Algorithm Flowchart for the assignation of the triggering diameter to every pore (*46*).

In pseudo-code, the simulation code can be written as follows:

```
Generate Pore Network Model
Find desorption triggering diameter for each pore
FOR P_relative= 0 to 1
  FOR pore=1,N_pores
     Calculate the quantity of nitrogen inside the pore (Eq.(8) and Eq.(9))
     using the actual diameter (adsorption) or the triggering diameter
     (desorption)
  END FOR
END FOR
Print isotherm branch
```

3.3 Diffusion Simulation

The first and second Fick laws are used to simulate diffusion into each pore of the network.

$$J_i = -D_{eff} \frac{\partial C_{ip}}{\partial l} \tag{10}$$

Boundary conditions at each end of the pore depend on the position and the type of node the pore is connected to (see Table 3). For external nodes, the concentration is considered as constant, and a Dirichlet boundary condition is imposed. For the internal nodes connected to just one pore (blind pore), a Neumann boundary condition is implemented. For internal nodes linked to more than one pore, a Kirchhoff's flow boundary condition is used. This means that the concentration at the extreme of the pores connected to the same node must be the same.

Table 3. Boundary conditions

Node type	Border condition
External node	$C_{ip} = C_{ext}, \quad t \geq 0$
Internal node (blind pore)	$\frac{dc_i}{dl} = 0 \quad l = L_p$
Internal node	$\sum_0^z J_{i,n} S_{p,n} = 0$

The network was spatially discretized using the orthogonal collocation method (*49*). For the resolution of the algebro-differential equation system, the DASPAK routine was employed (*50*).

For diffusion simulation, a 3D semi-infinite pore network, representing an infinite plate, was used. Two orthogonal directions are periodic, while in the third direction, boundaries represent the entrance and the exit of the network. A similar element was presented before by Gladden in 1991 (*20*). For the calculation of the tortuosity factor, a methodology like the one presented by Ruthven in 1984 is implemented. At steady state, the molar flow at the exit of the network can be calculated as the addition of the molar flows coming out of each individual pore which is connected to the external nodes of the exit face of the infinite plate (11).

$$J_i = -D_m \frac{\sum Jip\, S_p}{\sum Sp}$$

(11)

The effective diffusion coefficient can be calculated assuming that the structure can be modelled in a higher length scale as a unique straight fluid macropore, where the concentration difference is measured between the inlet and the outlet of the 3D periodic network (equation 12). The length L_N represents the linear distance between the two non-periodic faces of the plate. Finally, by definition, the tortuosity can be calculated using the equation *(3)*.

$$J_i = -D_{eff} \frac{\Delta C_i}{L_N}$$

(12)

4. Results

The final simulated isotherm is the average of the characterization of 50 different 3D distorted hierarchical pore networks generated with the same input parameters. A randomly distorted cubic lattice was used for the generation of the networks. The type of lattice fixed the maximum connectivity to 6. The experimental sorption curves were fitted using three porosity levels with three different pore size distributions (PSD 1, PSD 2, and PSD 3). Each pore size distribution has its own grid spacing and pore existence probability (PEP). The length of the pores is defined by the position of the lattice points. A cubic section of one of the full pore networks is shown in Figure 5.

Figure 5. Cubic section of one of the full networks

The parameters of the pore network model were identified by using a particle swarm optimization (PSO) algorithm. The resulting pore network model provides a digital characterization isotherm in good agreement with the experimental isotherm (Figure 6). To validate the pore network model, the digital scanning curves were compared to experimental ones. Overall, a good agreement was observed (Figure 7). The final parameters for the pore network generation model are listed in Table 4.

The adsorption isotherm is the easiest branch to fit. It allows one to set the pore volume distribution of the structure. However, to fit the desorption isotherm and the scanning curves, the topology of the network plays an important role. It is computationally possible to generate pore network models with the same adsorption isotherm but with totally different desorption branches due to a different topology. This allows one to infer that this could also be possible experimentally and could explain why solids with similar textural properties can have very different experimental tortuosity values (*51, 52*). Complex pore networks exhibit hysteresis in different classic characterization techniques (Nitrogen Porosimetry, Mercury Porosimetry, CryoPorometry, and ThermoPorometry). In each of them, the pore network organization has been declared to be partially responsible for this. In the particular case of Nitrogen Porosimetry (*53*), during the desorption stage, there is a retention of nitrogen in a metastable

state within some pores. As explained above, the evaporation process is blocked by the nitrogen contained in pores with lower evaporation pressure that stand between the blocked pores and the vapor phase. As mentioned before, this phenomenon is called “pore blocking” or “pore shielding”. Pore blocking is related to a characteristic size effect and to how these pores are connected to each other. For complex solids as γ-alumina, the shape of the desorption isotherm is influenced by the topology of the network, and hence it contains implicit information about its topology. It is preferable to use the word “implicit” because, to relate the topology of the network to the shape of the isotherm, a model is needed. At this point, it is valid to mention also that if the desorption branch is influenced by the topology, it is then also heavily influenced by the volume distribution into space.

Table 4. Optimized parameters for the pore network generation

Lattice Type	**Dimensions**	**Grid spacing (m)**	**Number of porosity levels**	**Skeletal density of the solid (kg/m3)**
Cubic	50x50x50	3.00E-08	3	3.1d3

Pore Size Distribution 1

Beta Distribution β=0.5; α=2.4; Minimum diameter = 20 nm, Maximum diameter= 60 nm

PEP = 0.1

Grid Spacing = 3

Pore Size Distribution 2

Beta Distribution β =1; α =1 ; Minimum diameter = 1 nm, Maximum diameter= 20 nm

PEP= 0.95

Grid Spacing = 2

Pore Size Distribution 3

Log-Normal Distribution Average=6 nm; Standard Deviation= 3 nm

PEP= 1

Grid Spacing = 1

*** Max number of pores = 375000**

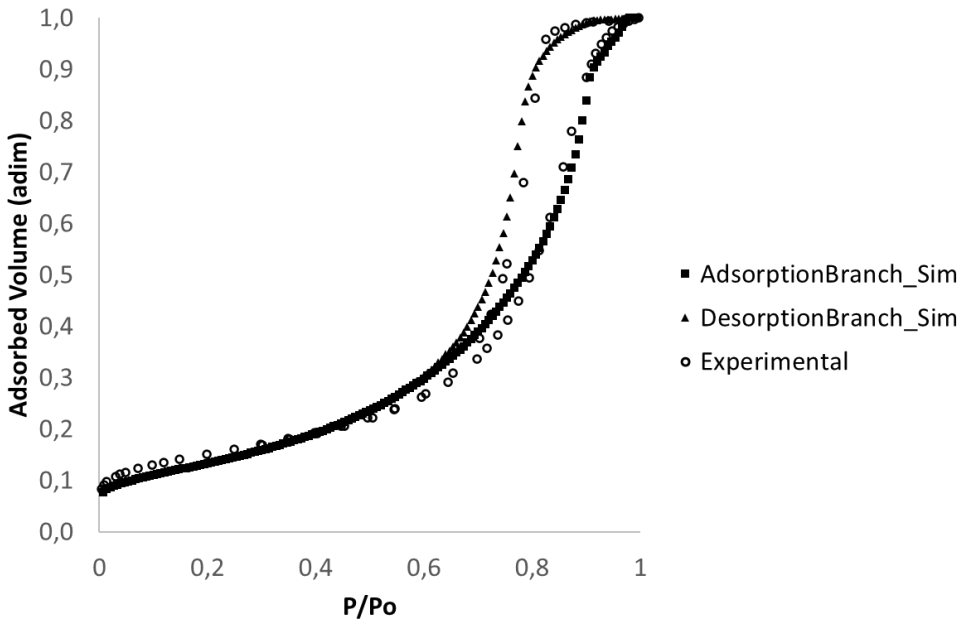

Figure 6. Experimental Isotherm compared to the simulated isotherm

In a single isotherm, there are 5 characteristics that are relevant for its interpretation: the slope that corresponds to the BET specific surface area, the pressure at which the hysteresis loop closes, the desorption branch slope (s) in the hysteresis loop, the relative pressure at which the desorption starts, and the volume of the total specific adsorbed nitrogen volume. The BET surface area slope represents the monolayer of the nitrogen adsorbed and is mainly determined by the smallest pores. In our digital twin, PSD 3 represents mainly small mesopores with some micropores. Hence, it is this PSD that determines the BET slope. The relative pressure at which the hysteresis loop closes is influenced mainly by PSD 1 and PSD 2. PSD 2 is a uniform pore size distribution that contains pores from 1 to 20 nm. The simulated isotherm loop closes at about 0.64 P/Po, just as the experimental curve (Figure 6). The different slopes in the desorption branch can indicate the presence of several pore populations. In the fitting of this section, all three pore size distributions have an important influence. However, the maximum connectivity, the pore existence probability for each population, and the grid spacing between populations play a very significant role. Indeed, these parameters modify the architecture of the network. They have also an important influence on the relative pressure at which the desorption starts. The parameters found for our digital twin also allow one to correctly predict the scanning curves

of the industrial alumina sample (Figure 7). This indicates that the digital twin is a good representation of the pore blocking effects of the network. Applying the BJH analysis to the desorption branch indicates the most accessible pore size, but an analysis of the scanning curves allows one to get information about how the pore populations are hindering each other. The scanning curves therefore provide more information about the internal organization of the network and constitute a very useful tool to computationally study the topology of the structure.

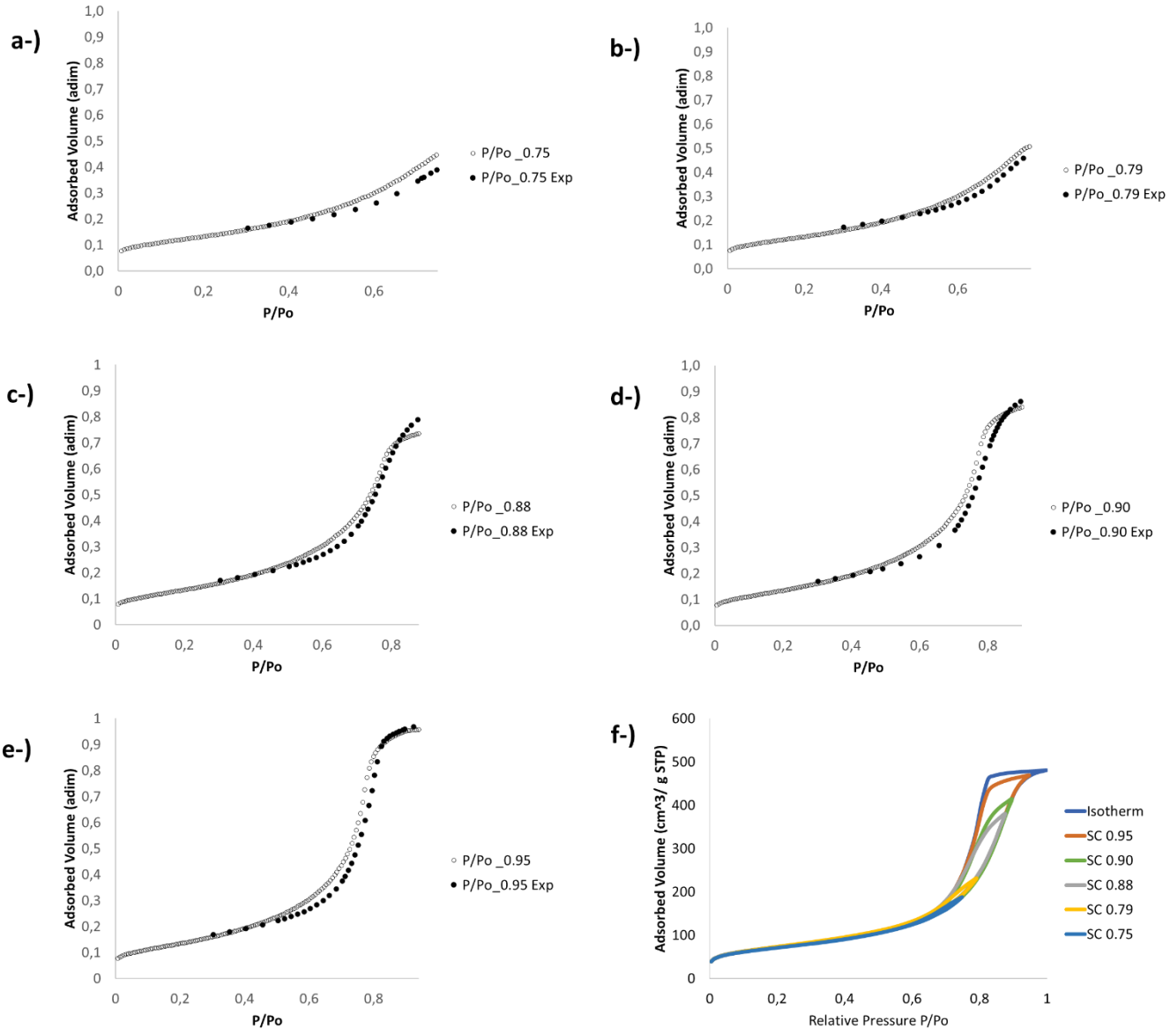

Figure 7. Experimental scanning curves compared to the simulated scanning curves: a-) Relative Pressure 0.75. b-) Relative Pressure 0.79. c-) Relative Pressure 0.88. d-) Relative Pressure 0.90. e-) Relative Pressure 0.95. f-) Experimental Scanning curves over the full experimental isotherm.

The overall pore size distribution in the pore network model contains <3% of pores with a pore diameter below 2 nm, representing less than 0.09 vol% of the total pore network. Figure 8 illustrates the combined input PSD of the pore network model on a volume basis. A BJH analysis was also applied to the digital isotherm. A good agreement was found between the BJH pore size distribution calculated for the experimental sample and the pore size distribution for pores above 10 nm (Figure 8). For pores smaller than 10 nm, the deviation is more pronounced.

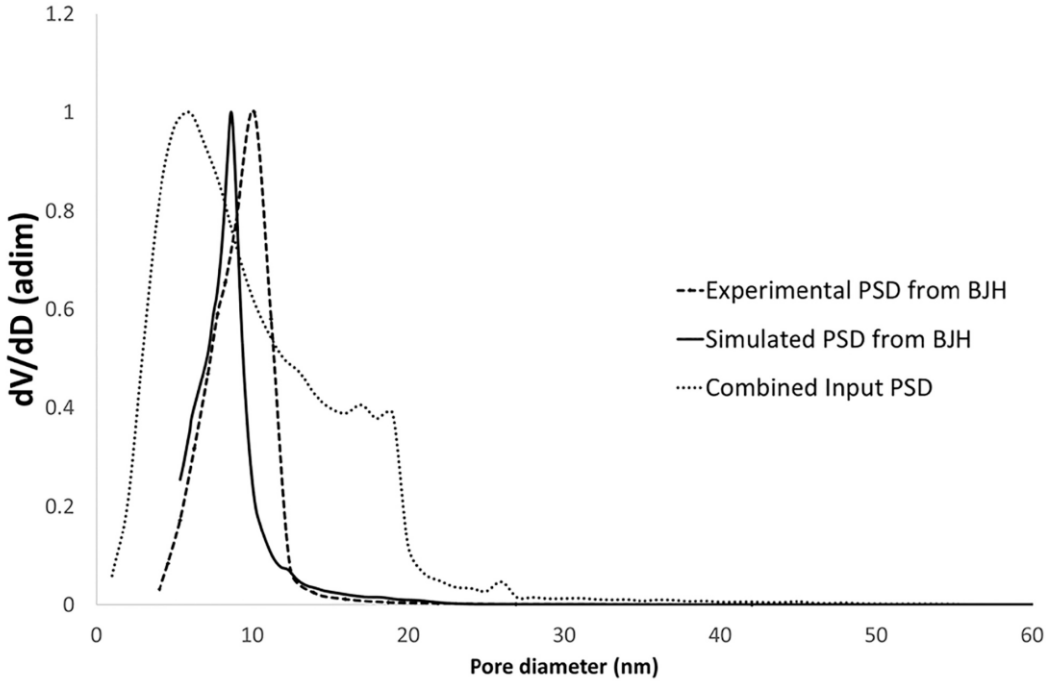

Figure 8. BJH pore size distribution comparison

Using diffusion simulations, a tortuosity factor equal to 1.5 was obtained. By employing PFG-NMR on the actual sample, an experimental tortuosity factor of 1.8 was measured. The relative error between the two tortuosity factors is 17 %.

5. Conclusions

A digital twin of an industrial alumina sample was created by generating a three-level hierarchical pore network model. Through parameter identification, a pore network model was obtained that provides a digital characterization isotherm in good agreement with the experimental isotherm. The same set of parameters allows one to correctly predict the nitrogen scanning curves, thereby validating the digital twin. The BJH pore size distribution obtained from the desorption branch of the digital isotherm corresponds well to the experimental BJH pore size distribution for the pores above 10 nm.

For nitrogen porosimetry, the adsorption isotherm mainly provides information on the pore volume distribution of the structure, but it does not allow one to get a statistically representative model that reproduces the effects of the topology of the solid. However, the desorption isotherm and the scanning curves are strongly influenced by the topology of the network. Therefore, it is computationally possible to have various representations with the same adsorption isotherm but with totally different desorption branches that represent different topologies. This allows us to infer that it should also be experimentally possible and could explain why solids with similar textural properties can have different experimental tortuosity values.

It should be stressed that it is not yet possible to confirm that, from a given isotherm, the attributes of the pore network structure curve can be uniquely identified. Our results point in the direction that a family of topologies can generate the same isotherms. However, the use of the scanning curves in the objective function of the optimizer could help to reduce the number of structures that can generate the same characteristic curves as a given alumina sample, and therefore restricts the possible topologies of the solid.

Diffusion simulations were carried out on the pore network model fitted to the nitrogen sorption curves. The predicted tortuosity factor differs by less than 20% from the tortuosity factor measured by PFG-NMR. This illustrates how a digital twin allows one to provide a reasonable estimate for the tortuosity factor from readily available nitrogen porosity experiments.

More information on the industrial alumina sample will of course allow one to generate better digital twins. Hence, the simulation tool will be extended to perform the structural optimization with an objective function that not only uses nitrogen porosimetry data, but also scanning curve, mercury porosimetry and NMR-cryoporometry simulations. In future works, further diffusion-reaction simulations will be used to investigate and better understand the link between the topology of these solids and their tortuosity.

6. References

1. Euzen P., Raybaud P. et al. *Handbook of Porous Solids*. *Alumina* 3, 2002.
2. Peter Matthews, G.; Ridgway, C. J.; Small, J. S. Modelling of simulated clay precipitation within reservoir sandstones. *Marine and Petroleum Geology [Online]* **1996,** *13* (5), 581–589.
3. Ezeuko, C. C.; Sen, A.; Grigoryan, A.; Gates, I. D. Pore-network modeling of biofilm evolution in porous media. *Biotechnology and bioengineering [Online]* **2011,** *108* (10), 2413–2423.
4. Huang, X.; Bandilla, K. W.; Celia, M. A. Multi-Physics Pore-Network Modeling of Two-Phase Shale Matrix Flows. *Transp Porous Med [Online]* **2016,** *111* (1), 123–141.
5. Li; Peters; Celia. Upscaling geochemical reaction rates using pore-scale network modeling. *Advances in Water Resources [Online]* **2006,** *29* (9), 1351–1370.
6. El Hannach, M.; Soboleva, T.; Malek, K.; Franco, A. A.; Prat, M.; Pauchet, J.; Holdcroft, S. Characterization of pore network structure in catalyst layers of polymer electrolyte fuel cells. *Journal of Power Sources [Online]* **2014,** *247*, 322–326.
7. Ye, G.; Duan, X.; Zhu, K.; Zhou, X.; Coppens, M.-O.; Yuan, W. Optimizing spatial pore-size and porosity distributions of adsorbents for enhanced adsorption and desorption performance. *Chemical Engineering Science [Online]* **2015,** *132*, 108–117.
8. Ye; Wang; Duan; Sui; Zhou; Coppens; Yuan. Pore network modeling of catalyst deactivation by coking, from single site to particle, during propane dehydrogenation. *AIChE J [Online]* **2019,** *65* (1), 140–150.
9. Hannaoui, R.; Horgue, P.; Larachi, F.; Haroun, Y.; Augier, F.; Quintard, M.; Prat, M. Pore-network modeling of trickle bed reactors: Pressure drop analysis. *Chemical Engineering Journal [Online]* **2015,** *262*, 334–343.
10. Fatt. The Network Model of Porous Media. *Society of Petroleum Engineers,* 1956.
11. Wheeler, A. Reaction Rates and Selectivity in Catalyst Pores; Advances in Catalysis; Elsevier, 1951; pp 249–327.

12. Cruz, M.; Mayagoitia, V.; Rojas, F. Mechanistic studies of capillary processes in porous media. Part 2.—Construction of porous networks by Monte-Carlo methods. *J. Chem. Soc., Faraday Trans. 1 [Online]* **1989,** *85* (8), 2079.
13. Mayagoitia, V.; Rojas, F.; Kornhauser, I.; Zgrablich, G.; Faccio. J; Gilot, B.; Guiglion, C. Refinements of the Twofold Description of Porous Media. *Langmuir [Online]* **1996,** *12* (1), 211–216.
14. Mayagoitia, V.; Rojas, F.; Kornhauser, I.; Pérez-Aguilar, H. Modeling of Porous Media and Surface Structures: Their True Essence as Networks. *Langmuir [Online]* **1997,** *13* (5), 1327–1331.
15. Riccardo, J. L.; Pereyra, V.; Zgrablich, G.; Rojas, F.; Mayagoitia, V.; Kornhauser, I. Characterization of energetic surface heterogeneity by a dual site-bond model. *Langmuir [Online]* **1993,** *9* (10), 2730–2736.
16. Mann; Golshan. Application of a stochastic network pore model to a catalyst pellet. *Chemical Engineering Communications [Online]* **1981,** *12* (4-6), 377–391.
17. Mann, R.; Thomson, G. Deactivation of a supported zeolite catalyst: Simulation of diffusion, reaction and coke deposition in a parallel bundle. *Chemical Engineering Science [Online]* **1987,** *42* (3), 555–563.
18. Androutsopoulos, G. P.; Salmas, C. E. A New Model for Capillary Condensation−Evaporation Hysteresis Based on a Random Corrugated Pore Structure Concept: Prediction of Intrinsic Pore Size Distributions. 1. Model Formulation. *Ind. Eng. Chem. Res. [Online]* **2000,** *39* (10), 3747–3763.
19. Spearing, M.; Matthews, G. P. Modelling characteristic properties of sandstones. *Transp Porous Med [Online]* **1991,** *6* (1), 71–90.
20. Hollewand, M. P.; Gladden, L. F. Modelling of diffusion and reaction in porous catalysts using a random three-dimensional network model. *Chemical Engineering Science [Online]* **1991,** *47* (7), 1761–1770.
21. Hollewand, M. P.; Gladden, L. F. Representation of porous catalysts using random pore networks. *Chemical Engineering Science [Online]* **1992,** *47* (9-11), 2757–2762.
22. Sadeghi, M. A.; Aghighi, M.; Barralet, J.; Gostick, J. T. Pore network modeling of reaction-diffusion in hierarchical porous particles: The effects of microstructure. *Chemical Engineering Journal [Online]* **2017,** *330*, 1002–1011.
23. Rieckmann, C.; Keil, F. J. Multicomponent Diffusion and Reaction in Three-Dimensional Networks: General Kinetics †. *Ind. Eng. Chem. Res. [Online]* **1997,** *36* (8), 3275–3281.
24. Sharratt, P. N.; Mann, R. Some observations on the variation of tortuosity with Thiele modulus and pore size distribution. *Chemical Engineering Science [Online]* **1987,** *42* (7), 1565–1576.
25. Nguyen, P. T. M.; Do, D. D.; Nicholson, D. On the Hysteresis Loop of Argon Adsorption in Cylindrical Pores. *J. Phys. Chem. C [Online]* **2011,** *115* (11), 4706–4720.
26. Bruschi, L.; Mistura, G.; Nguyen, P. T. M.; Do, D. D.; Nicholson, D.; Park, S.-J.; Lee, W. Adsorption in alumina pores open at one and at both ends. *Nanoscale [Online]* **2015,** *7* (6), 2587–2596.

27. Coasne, B.; Gubbins, K. E.; Pellenq, R. J.-M. A Grand Canonical Monte Carlo Study of Adsorption and Capillary Phenomena in Nanopores of Various Morphologies and Topologies: Testing the BET and BJH Characterization Methods. *Part. Part. Syst. Charact. [Online]* **2004,** *21* (2), 149–160.

28. Palmer, J. C.; Brennan, J. K.; Hurley, M. M.; Balboa, A.; Gubbins, K. E. Detailed structural models for activated carbons from molecular simulation. *Carbon [Online]* **2009,** *47* (12), 2904–2913.

29. Kolesnikov, A. L.; Budkov, Y. A.; Gor, G. Y. Adsorption-induced deformation of mesoporous materials with corrugated cylindrical pores. *The Journal of Chemical Physics [Online]* **2020,** *153* (19), 194703.

30. Armatas, G. S.; Pomonis, P. J. A Monte Carlo pore network for the simulation of porous characteristics of functionalized silica: Pore size distribution, connectivity distribution and mean tortuosities. *Chemical Engineering Science [Online]* **2004,** *59* (24), 5735–5749.

31. López-Ramón, M. V.; Jagiełło, J.; Bandosz, T. J.; Seaton, N. A. Determination of the Pore Size Distribution and Network Connectivity in Microporous Solids by Adsorption Measurements and Monte Carlo Simulation. *Langmuir [Online]* **1997,** *13* (16), 4435–4445.

32. Meyers, J.; Nahar, S.; Ludlow, D.; Liapis, A. Determination of the pore connectivity and pore size distribution and pore spatial distribution of porous chromatographic particles from nitrogen sorption measurements and pore network modelling theory. *Journal of Chromatography A [Online]* **2001,** *907* (1-2), 57–71.

33. Murray, K. L.; Seaton, N. A.; Day, M. A. Use of Mercury Intrusion Data, Combined with Nitrogen Adsorption Measurements, as a Probe of Pore Network Connectivity. *Langmuir [Online]* **1999,** *15* (23), 8155–8160.

34. Seaton, N. A. Determination of the connectivity of porous solids from nitrogen sorption measurements. *Chemical Engineering Science [Online]* **1991,** *46* (8), 1895–1909.

35. Perkins, E. L.; Lowe, J. P.; Edler, K. J.; Tanko, N.; Rigby, S. P. Determination of the percolation properties and pore connectivity for mesoporous solids using NMR cryodiffusometry. *Chemical Engineering Science [Online]* **2008,** *63* (7), 1929–1940.

36. Rojas, F.; Kornhauser, I.; Felipe, C.; Esparza, J. M.; Cordero, S.; Domínguez, A.; Riccardo, J. L. Capillary condensation in heterogeneous mesoporous networks consisting of variable connectivity and pore-size correlation. *Phys. Chem. Chem. Phys. [Online]* **2002,** *4* (11), 2346–2355.

37. Kikkinides, E. S.; Monson, P. A.; Valiullin, R. Sorption Isotherm Reconstruction and Extraction of Pore Size Distributions for Serially Connected Pore Model (SCPM) Structures Employing Algorithmic and Statistical Models. *J. Phys. Chem. C [Online]* **2020,** *124* (39), 21591–21607.

38. Gommes, C. J. Adsorption, capillary bridge formation, and cavitation in SBA-15 corrugated mesopores: a Derjaguin-Broekhoff-de Boer analysis. *Langmuir : the ACS journal of surfaces and colloids [Online]* **2012,** *28* (11), 5101–5115.

39. Wood, J.; Gladden, L. F.; Keil, F. J. Modelling diffusion and reaction accompanied by capillary condensation using three-dimensional pore networks. Part 2. Dusty gas model and general reaction kinetics. *Chemical Engineering Science [Online]* **2002,** *57* (15), 3047–3059.

40. Johannessen, E.; Wang, G.; Coppens, M.-O. Optimal Distributor Networks in Porous Catalyst Pellets. I. Molecular Diffusion. *Ind. Eng. Chem. Res. [Online]* **2007,** *46* (12), 4245–4256.

41. Ye, G.; Wang, H.; Zhou, X.; Keil, F. J.; Coppens, M.-O.; Yuan, W. Optimizing catalyst pore network structure in the presence of deactivation by coking. *AIChE J. [Online]* **2019,** *65* (10), 277.

42. Ye, G.; Zhou, X.; Yuan, W.; Coppens, M.-O. Probing pore blocking effects on multiphase reactions within porous catalyst particles using a discrete model. *AIChE J. [Online]* **2016,** *62* (2), 451–460.

43. Wang, H. Morphological Modelling and Transport Properties of Mesoporous Alumina; l'Université de recherche Paris Sciences et Lettres, France, 2017.

44. Rigby, S. P.; Hasan, M.; Stevens, L.; Williams, H. E. L.; Fletcher, R. S. Determination of Pore Network Accessibility in Hierarchical Porous Solids. *Ind. Eng. Chem. Res. [Online]* **2017,** *56* (50), 14822–14831.

45. Rigby, S. P.; Fletcher, R. S.; Raistrick, J. H.; Riley, S. N. Characterisation of porous solids using a synergistic combination of nitrogen sorption, mercury porosimetry, electron microscopy and micro-focus X-ray imaging techniques. *Phys. Chem. Chem. Phys. [Online]* **2002,** *4* (14), 3467–3481.

46. G. Ledezma , J. Verstraete, L. Sorbier, D. Leinekugel-Le Cocq, E. Jolimaitre, C Jallut. Computational Characterization of a Pore Network Model by Using a Fast Nitrogen Porosimetry Simulation. In *31st European Symposium on Computer Aided Process Engineering*; Metin Türkay Rafiqul Gani, Ed. 50; Elsevier, 2021.

47. Gelb, L. The ins and outs of capillary condensation in cylindrical pores. *Molecular Physics [Online]* **2009,** *100* (13), 2049–2057.

48. Zeng, Y.; Prasetyo, L.; Tan, S. J.; Fan, C.; Do, D. D.; Nicholson, D. On the hysteresis of adsorption and desorption of simple gases in open end and closed end pores. *Chemical Engineering Science [Online]* **2017,** *158*, 462–479.

49. Villadsen, J. V.; Stewart, W. E. Solution of boundary-value problems by orthogonal collocation. *Chemical Engineering Science [Online]* **1967,** *22* (11), 1483–1501.

50. van Keken, P. E.; Yuen, D. A.; Petzold, L. R. DASPK: A new high order and adaptive time-integration technique with applications to mantle convection with strongly temperature-and pressure-dependent rheology. *Geophysical & Astrophysical Fluid Dynamics [Online]* **1995,** *80* (1-2), 57–74.

51. Ferreira. Modélisation du transport intragranulaire dans un réacteur catalytique; Université Claude Bernard - Lyon 1, France, 2018.

52. Kolitcheff. Approche multitechnique des phénomènes de diffusion en hydrotraitement de distillats; Université Claude Bernard - Lyon 1, France, 2017.

53. Rouquerol, F.; Rouquerol, J.; Sing, K. S. W. The Experimental Approach. In *Handbook of porous solids*; Schüth, F., Ed.; Wiley-VCH: Weinheim, 2002; pp 236–275.